

Faradaic efficiency of O₂ evolution on metal nanoparticle sensitized hematite photoanodes

Cite this: *Phys. Chem. Chem. Phys.*,
2014, **16**, 1271

Beniamino Iandolo,^{*a} Björn Wickman,^{ab} Brian Seger,^b Ib Chorkendorff,^b Igor Zorić^a
and Anders Hellman^a

Functionalization of transition metal oxides using metallic nanoparticles is an interesting route towards efficient photoelectrochemical hydrogen production via water splitting. Although an enhanced photocurrent in photoanodes upon functionalization with metallic nanostructures has been observed in several studies, to the best of our knowledge no measurements of the Faradaic efficiency (FE) of the oxygen evolution reaction (OER) have been reported for such systems. This work characterizes the FE on a model system consisting of ultra-thin films of hematite (Fe₂O₃) sensitized with Ti/Au nanodisks. Compared to bare hematite references, sensitized samples showed significantly enhanced photocurrents as well as O₂ evolution. Experimental evidence suggests that the observed enhancement was not due to photocatalytic activity of the nanodisks. The FE has been determined to be 100%, within the experimental errors, for both sensitized and reference samples. Also, this work demonstrates that the sensitized samples were stable for at least 16 hours photocurrent testing. The concepts shown in this work are generally applicable to any situation in which a semiconductor has its water splitting performance enhanced by metallic nanostructures.

Received 10th October 2013,
Accepted 12th November 2013

DOI: 10.1039/c3cp54288b

www.rsc.org/pccp

Introduction

Photoelectrochemical (PEC) water splitting is appealing for large-scale solar to chemical energy conversion.¹ Transition metal oxides, such as TiO₂, WO₃, ZnO and Fe₂O₃, have been thoroughly explored as light absorber materials in PEC cells over the past few decades.^{2–6} Fe₂O₃ (hematite) is considered particularly promising because it is an abundant, inexpensive semiconductor that is able to absorb two thirds of the visible solar light (thanks to its bandgap of around 2 eV) and is able to resist (photo)corrosion in an electrolytic environment of pH > 3 (ref. 7). However, the present energy conversion efficiency of hematite-based PEC cells falls well below the predicted theoretical maximum⁸ due to a combination of factors, including: (i) a low absorption coefficient for photon energies close to the bandgap,⁹ (ii) a short lifetime of excited carriers,¹⁰ (iii) an extremely short hole diffusion length of 2–4 nm,¹¹ and (iv) sluggish O₂ evolution kinetics.¹²

Functionalization of the surface of hematite with overlayers and/or nanostructures has recently attracted interest as a promising strategy to tackle some of the aforementioned issues. Upon surface modification, hematite's photocurrent has been shown to increase as a result of improved charge separation

due to p–n homojunctions¹³ and as a result of reduced OER overpotential.^{14–18} The latter effect has been rationalized in terms of reduced charge recombination close to the hematite/electrolyte interface^{14,15} or from increased hole transfer across the same interface.^{16–18}

The addition of metallic nanostructures has also been investigated,^{19–21} with beneficial effects including: (i) enhanced charge generation, (ii) increased conductivity in hematite upon excitation of plasmonic resonances in the metal, and (iii) improved charge separation thanks to Schottky barrier formation at the hematite/metal interface.²²

We have observed a considerable photocurrent increase in our model photoanodes consisting of ultra thin hematite films upon addition of Ti/Au nanodisks.²³ Spectrally resolved measurements and calculations indicate that the observed improvement can be divided into two contributions. For photon energies close to the bandgap in hematite, excitation of localized plasmons results in an electric field enhancement around the nanoparticles leading to increased generation of electron–hole pairs. At higher photon energies, where the plasmons are not excited, the improvement is likely to be related to passivation of surface states resulting in reduced charge recombination close to the electrolyte.¹⁵

However, the amount of O₂ evolved during the OER was not measured directly, and thus it was not proven that the increased photocurrent actually led to an increased O₂ production. It should be stressed that one needs to be careful when analyzing results solely based on the measured photocurrent since, in principle,

^a Department of Applied Physics, Chalmers University of Technology, SE-421 96 Göteborg, Sweden. E-mail: iandolo@chalmers.se

^b Center for Individual Nanoparticle Functionality, Department of Physics, Technical University of Denmark, DK-2800 Lyngby, Denmark

a substantial part of the current can originate from other oxidation reactions (e.g. corrosion).²⁴ This is especially important when performing dynamic measurements, such as linear sweep or cyclic voltammetry. Such measurements should always be complemented by static tests and preferably also detection and quantification of the product, in this case O₂. The Faradaic efficiency of the evolution of a certain reaction product is defined as the ratio between the charge corresponding to the amount of product evolved and the total charge consumed during the reaction. In the present case, by quantifying the amount of evolved O₂ (using a gas chromatograph) and comparing it with the charge corresponding to the photocurrent during the reaction, one can determine the FE of the OER.

A systematic investigation of the FE of the OER is currently lacking in metal/catalysts enhanced photoelectrochemistry.^{25–28} In the present work, we perform such investigations and answer the questions if, and to what extent the increased photocurrent seen on hematite photoanodes sensitized with Ti/Au nanodisks results in an increased O₂ production. In addition, we answer the question whether the Au nanodisks operate as an active co-catalyst for the OER reaction under the considered conditions.

Methods

All the photoanodes were fabricated on indium tin oxide (ITO) covered glass substrates (PGO GmbH, ITO thickness of 120 nm and sheet resistance of $\leq 15 \Omega \text{ sq}^{-1}$). The fabrication procedure is described in detail elsewhere.²¹ In short, Fe films were deposited on the ITO by physical vapor deposition (base pressure $< 5 \times 10^{-7}$ mbar) followed by thermal oxidation for 6 h at 350 °C in a mixed N₂/O₂ (72/28% respectively) atmosphere, which led to complete conversion of Fe into Fe₂O₃. The thickness of the Fe₂O₃ films was determined to be 25 ± 1.7 nm from surface profiler measurements. Arrays of Ti/Au nanodisks, with short range order, were deposited on top of the Fe₂O₃ films *via* hole-mask colloidal lithography.²⁹ The nanodisks had an average diameter of 50 nm, a total height of 30 nm and a surface coverage of *ca.* 5% as confirmed by SEM inspection. The nanodisk thickness consisted of 5 nm of Ti and 25 nm Au, subsequently evaporated in the same run. The Ti layer was deposited in order to improve the adhesion between Fe₂O₃ and Au. Samples with Ti nanodisks only were also produced that were identical to these, except that no Au was deposited.

Current *vs.* potential measurements were carried out in a standard three-electrode configuration using a H-type glass cell with working electrode and counter-electrode compartments separated by a glass frit. The working electrode compartment had flat optical windows to allow illumination of the samples.³⁰ The fabricated photoanodes were used as a working electrode, a Pt wire as a counter electrode, and a saturated calomel electrode (SCE) as a reference electrode. The electrolyte was a 0.1 M KOH solution (pH = 12.9) continuously purged with Ar. The potential scale was converted to the reversible hydrogen electrode (RHE) scale through the formula $E_{\text{RHE}} = E_{\text{SCE}} + E_{\text{SCE}}^0 + 0.059 \text{ pH}$, where E_{SCE} is the measured potential and $E_{\text{SCE}}^0 = 0.241 \text{ V}$ at 25 °C for a SCE.

The samples were illuminated from the front side during all measurements. Cyclic voltammetry at a scan rate of 10 mV s^{-1} was carried out using a Bio-Logic Instruments' VMP2 potentiostat. Sunlight was simulated using a 150 W Xe lamp (Newport) and an AM 1.5 filter, adjusting the power density to 100 mW cm^{-2} at the sample surface using an RPS900-R spectrophotometer (International Light).

The photocurrent *vs.* time traces were recorded at a constant potential of 1.56 V *vs.* RHE. O₂ quantification was carried out using a gas chromatograph (Agilent Technologies, 7890A) equipped with a thermal conductivity detector and automated gas sampling. A diaphragm pump (KNF, NF5RPDCB-4) was used to keep the gas in the working electrode compartment flowing at a rate of about 30 mL min^{-1} through the GC sample loop and bubbling through the electrolyte. The pressure in the head space of the working electrode compartment was adjusted to atmospheric pressure. Before the reactions, the working electrode compartment was flushed with Ar and the cell was closed off. After each reaction, the gas concentrations were allowed to equilibrate for 2.5 min before a gas sample was injected into the GC to determine the O₂ concentration. A gas mixture of known concentration (0.996% vol. O₂ in Ar) was used to calibrate the O₂ signal. The number of moles of O₂, n_{O_2} , was then extracted using the ideal gas law. The gas volume in the working electrode compartment was determined electrochemically by performing hydrogen evolution on a Pt wire in 0.1 M HClO₄ and quantifying the produced H₂ concentration using the same GC. Finally, the corresponding charge, Q_{O_2} , was obtained *via* the equation $Q_{\text{O}_2} = 4Fn_{\text{O}_2}$, where F is the Faraday constant.

The photocurrent *vs.* wavelength measurements were carried out using the same three electrode configuration as above, in a custom made polyether ether ketone (PEEK) cell. A constant bias of 1.5 V *vs.* RHE was applied using a Gamry Reference 600 potentiostat. Light from a 100 W quartz tungsten halogen lamp was guided into a Cornerstone 130 1/8 m monochromator (Oriel). A glass filter (FSR-GG400, Newport) was used to cut-off wavelengths shorter than 400 nm.

Scanning electron microscopy and energy dispersive X-rays spectroscopy (SEM/EDX) were performed using a Zeiss Supra 60 VP SEM on sensitized photoanodes before and after long term measurements. SEM micrographs were recorded with an acceleration voltage of 5 keV, while EDX spectra were acquired at 20 keV. The elemental analysis was performed on 5 spots before and after the test, and the average Fe, Ti and Au atomic content was used to determine the Fe/Ti and Fe/Au ratios. The error bars of the Fe/Ti and Fe/Au ratios were determined using standard error propagation.

Results

The photoanodes sensitized with the Ti/Au nanodisks consistently showed a higher photoactivity when compared to reference samples of bare hematite films of the same thickness. Fig. 1 compares the current density *vs.* potential – or $J(V)$ – curves for a sensitized and a reference sample with a hematite thickness of

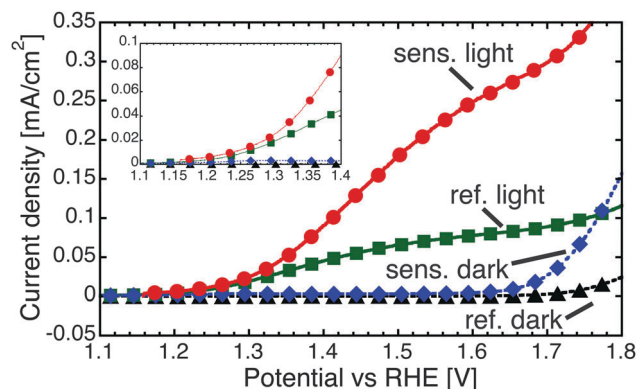


Fig. 1 $J(V)$ scans of 25 nm thick Fe_2O_3 reference and $\text{Fe}_2\text{O}_3 + \text{Ti/Au}$ nanodisks sensitized hematite samples in the dark (triangles and diamonds respectively) and under solar simulated illumination (squares and circles). The inset shows the onset potential region, which is approximately 1.22 V vs. RHE for both reference and sensitized samples.

25 nm, under dark conditions and under solar simulated illumination. The photocurrent of the sensitized sample is significantly larger than the reference sample, with an enhancement factor of 3 or higher for potentials higher than 1.5 V vs. RHE. Both reference and sensitized samples show negligible dark currents for the majority of the potential window. At the most anodic potentials, an increased current was observed for both samples. For the sensitized samples the onset was approximately 1.66 V vs. RHE and the slope was higher than for the reference. This is likely a result of electrochemical O_2 evolution on the surface of the Au nanodisks.³¹

Wavelength dependent photocurrent measurements were performed at 1.5 V vs. RHE under illumination on bare Fe_2O_3 , $\text{Fe}_2\text{O}_3 + \text{Ti}$, and $\text{Fe}_2\text{O}_3 + \text{Ti/Au}$ photoanodes. The results are summarized in Fig. 2, which shows for both $\text{Fe}_2\text{O}_3 + \text{Ti/Au}$ and $\text{Fe}_2\text{O}_3 + \text{Ti}$ samples the difference between the photocurrent in the sensitized sample $J_{\text{sens}}(\lambda)$ and the reference sample $J_{\text{ref}}(\lambda)$, normalized to the reference photocurrent $J_{\text{ref}}(\lambda)$, i.e. $(J_{\text{sens}}(\lambda) - J_{\text{ref}}(\lambda))/J_{\text{ref}}(\lambda)$. For the $\text{Fe}_2\text{O}_3 + \text{Ti/Au}$ sample, the signature of

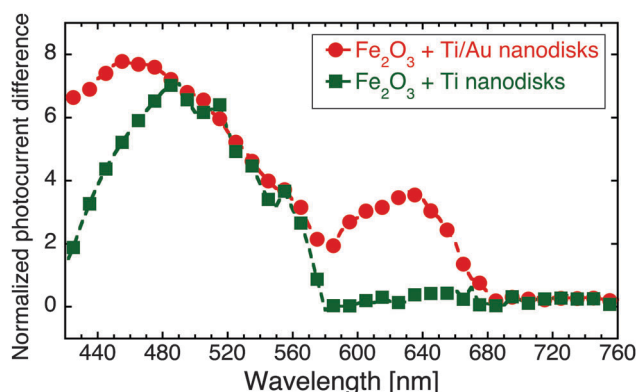


Fig. 2 Normalized photocurrent difference, measured as a function of photon wavelength: (i) between a $\text{Fe}_2\text{O}_3 + \text{Ti/Au}$ nanodisk sample and a bare Fe_2O_3 film (circles), and (ii) between a $\text{Fe}_2\text{O}_3 + \text{Ti}$ nanodisk sample (squares) and the same Fe_2O_3 film.

a localized plasmon induced photocurrent improvement is present in the form of a peak in the wavelength region between 600 and 680 nm (for further discussion see ref. 22). The plasmonic contribution to the photocurrent increase was estimated by first integrating $J_{\text{ref}}(\lambda)$ in the whole spectral region investigated, and then by integrating $J_{\text{sens}}(\lambda)$ over both the whole spectrum and for $600 < \lambda < 680$ nm. The ratio between the integrated plasmonic photocurrent and the total photocurrent increase was then determined to be about 10%. While this feature is completely missing (as expected) for the $\text{Fe}_2\text{O}_3 + \text{Ti}$ sample, both $\text{Fe}_2\text{O}_3 + \text{Ti/Au}$ and $\text{Fe}_2\text{O}_3 + \text{Ti}$ photoanodes show almost the same increased performance between 600 and 480 nm. The $\text{Fe}_2\text{O}_3 + \text{Ti/Au}$ sample also shows a higher improvement for the shortest wavelengths measured. The mechanism of photocurrent enhancement for $\lambda < 600$ nm is likely to be connected with passivation of surface states at the semiconductor/electrolyte interface.¹⁵ Further discussion is beyond the scope of this work.

By inspecting the $J(V)$ and $J(\lambda)$ plots, it is possible to rule out the possibility that, under illumination and at potentials lower than ~ 1.6 V vs. RHE, Au is acting as a photoelectrocatalyst for the OER. This is based on the following observations: (i) the onset potential is about 1.22 V vs. RHE for both samples, as shown in the inset of Fig. 1; (ii) the $J(\lambda)$ plot shows that the photocurrent enhancement has a spectral dependence for the $\text{Fe}_2\text{O}_3 + \text{Ti/Au}$ sample, which should not be present if the Au nanodisks were acting as pure photocatalysts for the OER; (iii) the $\text{Fe}_2\text{O}_3 + \text{Ti}$ sample without the Au shows a considerable photocurrent increase for $\lambda < 600$ nm.

In order to quantify the FE on the photoanodes, measurements of the evolved O_2 were performed using a gas chromatograph (GC) and the corresponding charge, Q_{O_2} , was compared to the total charge, Q_{tot} , obtained by integration of the PEC current, measured at 1.56 V vs. RHE. This value corresponds to 0.5 V vs. SCE and is sufficiently more cathodic than the potential at which the dark current starts to become significant, as well as sufficiently more anodic than the onset potential of the photocurrent in order to see an appreciable difference in photoresponse between sensitized and reference samples. Finally, the FE was determined as the ratio $Q_{\text{O}_2}/Q_{\text{tot}}$. Fig. 3 summarizes the results from the experimental O_2 quantification and the integrated photocurrents, with Q_{O_2} and Q_{tot} and their respective FE's plotted as a function of reaction time for a sensitized $\text{Fe}_2\text{O}_3 + \text{Ti/Au}$ sample and a reference sample. The calculated charge from the O_2 detection follows closely the one from the photocurrent and as a result, the FE is close to unity for both samples. It is worth mentioning that O_2 dissolved in the electrolyte is not measured by the GC, which can result in an underestimation of Q_{O_2} and therefore of the FE. However, the electrolyte in the working electrode compartment was continuously bubbled with the circulating gas in the head space, which means that we can assume that the dissolved O_2 is in equilibrium with the gas phase O_2 . According to Henry's law (assuming a Henry's coefficient for O_2 in water of $7.794 \times 10^4 \text{ Pa m}^3 \text{ mol}^{-1}$ (ref. 32)), the concentration of O_2 in the liquid phase should be about two orders of magnitude lower than that

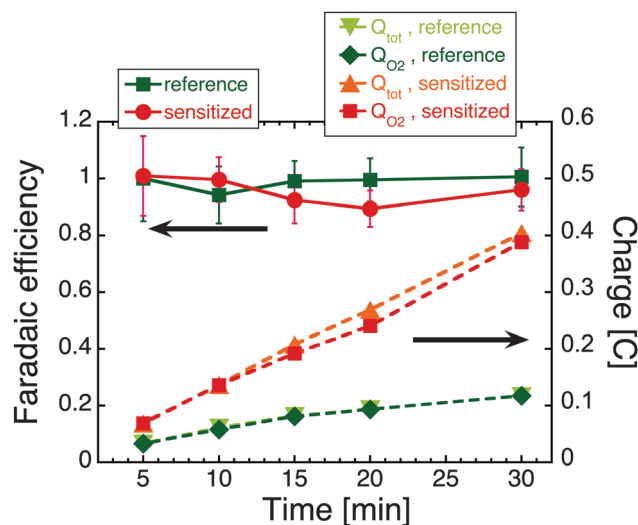


Fig. 3 Faradaic efficiency of the OER on reference and Ti/Au nanodisks sensitized (full lines, left y-axis) and comparison between the charges Q_{O_2} and Q_{tot} obtained from GC measurements and integration of the photocurrent respectively (dashed lines, right y-axis). Measurements were carried out at 1.56 V vs. RHE under solar simulated illumination.

in the gas phase. Since the liquid and gas volumes of the working electrode compartment were similar, the amount of O_2 dissolved in the electrolyte can be neglected.

Further uncertainties when measuring the amount of O_2 produced include the determination of gas volume and pressure in the working electrode compartment, as well as the amount of O_2 that leaked into the setup, *i.e.* not originating from the water splitting reaction. The latter was corrected for by analyzing the intensity of the N_2 peak in the GC and using the O_2/N_2 ratio determined from leak testing (corresponding to air composition). The rate of O_2 (and N_2) leaking into the system was much lower than the rate of O_2 evolution on the samples at 1.56 V vs. RHE upon broadband illumination. The error bars in Fig. 3 represent the spread of data from the O_2 calibration and the O_2/N_2 ratio from leak tests. Taking the experimental errors into consideration, we consider the results in Fig. 3 to be strong evidence that the FE of O_2 evolution is unity, for both reference and sensitized samples.

It is worth mentioning that the O_2 leak rate turned out to be comparable to the O_2 evolution rate upon monochromatic illumination obtained by filtering the light from the Xe lamp. This fact prevented an accurate wavelength resolved measurement of the FE on our samples. Nonetheless, we can assign a one-to-one correspondence between increase in photocurrent and an increase in O_2 evolution at all wavelengths upon decoration of hematite with the nanodisks, since the measured FE encompasses all wavelengths. Moreover, hematite is reported to be stable⁷ at the values of applied potential and electrolyte pH used for these measurements, which excludes the possibility of O_2 evolution from photo-corrosion of Fe_2O_3 .

16 h long photocurrent measurements were performed under the same conditions as described for the FE test (1.56 V vs. RHE, solar simulated illumination) to investigate the PEC stability of

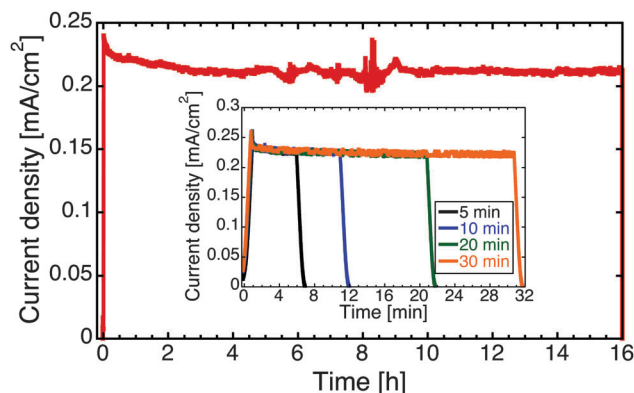


Fig. 4 Stability test on a Ti/Au nanodisks sensitized sample during solar simulated illumination at 1.56 V vs. RHE for 16 h. The inset shows shorter timespan photocurrent measurements on the same sample, used for the determination of the FE presented in Fig. 3.

the $Fe_2O_3 + Ti/Au$ samples. As shown in Fig. 4, the photocurrent stabilized after approximately 2 hours and did not decay further over the remaining 14 hours. The inset shows the shorter photocurrent vs. time traces used for the determination of the FE data presented in Fig. 3. The O_2 charge measured by the GC after the 16 hours run yielded a FE of 0.989.

The morphology of the sample before and after the test was compared through SEM and EDX characterization. The top-view SEM micrographs in Fig. 5a and b indicate that the surface coverage by the Ti/Au nanodisks remained unchanged. Furthermore, the EDX data in Fig. 5c show that the Fe:Ti and Fe:Au ratio is the same within the measurement error, thus proving that the nanodisks did not undergo corrosion during the stability test. These results offer further proof that the observed photocurrent goes solely into O_2 production from water splitting.

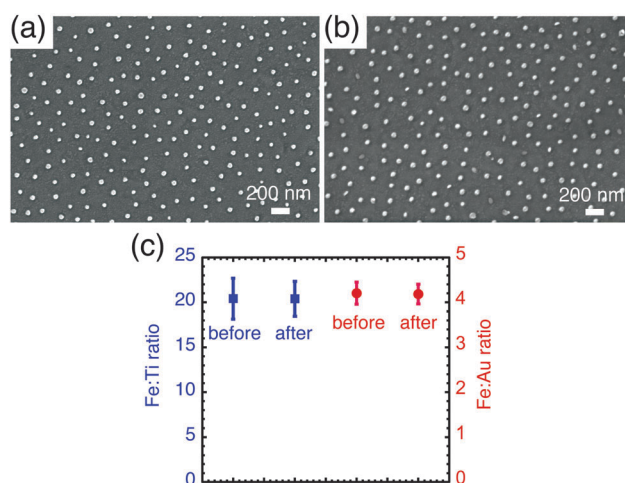


Fig. 5 SEM/EDX characterization of a $Fe_2O_3 + Ti/Au$ sample before and after the stability test. (a) and (b) Top view SEM image of the sample before and after the 16 h photocurrent measurement respectively. (c) EDX based comparison between the atomic Fe/Ti and Fe/Au atomic ratios before and after the test (squares and circles, respectively).

Conclusions

In conclusion, we investigated the FE of the OER at the surface of thin-film based metal oxide photoanodes, using ultra-thin hematite films sensitized with Ti/Au nanodisks as a model system. We showed a significant enhancement of the photocurrent in hematite upon addition of the nanodisks, with strong evidence that the Au does not act as a photocatalyst for the OER at potentials less anodic than ~ 1.6 V vs. RHE. We determined a FE of 1 ± 0.08 for both sensitized and reference samples. No detectable signs of corrosion of the sensitized photoanodes were observed, nor other reaction products were detected during a 16 hours long photocurrent measurement under simulated solar illumination. These results indicate a one-to-one correspondence between an increase in photocurrent and an increase in the amount of O₂ produced at the photoanode surface upon functionalization with Ti/Au nanodisks. Metal nanostructures enhanced water splitting is a relatively new, exciting field within photoelectrochemistry, and the findings presented here are of interest to improve the understanding of any system where the PEC properties of metal oxides (being Fe₂O₃, TiO₂, ZnO or others) are improved with the help of metallic nanostructures.

Acknowledgements

BI, IZ and BW thank Formas (project numbers 219-2011-959 and 229-2009-772) for financial support. AH acknowledges the Swedish Research Council.

References

- 1 US Department of Energy, Basic Research Needs for Solar Energy Utilization (updated report), 2010.
- 2 A. Fujishima and K. Honda, *Nature*, 1972, **238**, 37.
- 3 A. Fujishima, X. Zhang and D. Tryk, *Surf. Sci. Rep.*, 2008, **63**, 515.
- 4 R. Van de Krol, Y. Liang and J. Schoonman, *J. Mater. Chem.*, 2008, **18**, 2311.
- 5 K. Sivula, F. Le Formal and M. Grätzel, *ChemSusChem*, 2011, **4**, 432.
- 6 K. L. Hardee and A. J. Bard, *J. Electrochem. Soc.*, 1976, **123**, 1024.
- 7 L. R. S. Yeh and N. Hackerman, *J. Electrochem. Soc.*, 1977, **124**, 833.
- 8 A. B. Murphy, P. R. F. Barnes, L. K. Randeniya, I. C. Plumb, I. E. Grey, M. D. Horne and J. Glasscock, *Int. J. Hydrogen Energy*, 2006, **31**, 1999.
- 9 I. Balberg and H. L. Pinch, *J. Magn. Magn. Mater.*, 1978, **7**, 12.
- 10 A. G. Joly, J. R. Williams, S. A. Chambers, G. Xiong, W. P. Hess and D. M. Laman, *J. Appl. Phys.*, 2006, **99**, 053521.
- 11 J. H. Kennedy and K. W. Frese, *Electrochem. Soc.*, 1978, **125**, 709.
- 12 B. Klahr, S. Gimenez, F. Fabregat-Santiago, T. Hamann and J. Bisquert, *J. Am. Chem. Soc.*, 2012, **134**, 4294.
- 13 Y. Lin, Y. Xu, M. T. Mayer, Z. I. Simpson, G. McMahon, S. Zhou and D. Wang, *J. Am. Chem. Soc.*, 2012, **134**, 5508–5511.
- 14 T. Hisatomi, F. Le Formal, M. Cornuz, J. Brillet, N. Tetreault, K. Sivula and M. Grätzel, *Energy Environ. Sci.*, 2011, **4**, 2512.
- 15 M. Barroso, C. A. Mesa, S. R. Pendlebury, A. J. Cowan, T. Hisatomi, K. Sivula, M. Grätzel, D. R. Klug and J. R. Durrant, *Proc. Natl. Acad. Sci. U. S. A.*, 2012, **109**, 15640.
- 16 S. D. Tilley, M. Cornuz, K. Sivula and M. Grätzel, *Angew. Chem., Int. Ed.*, 2010, **49**, 6405.
- 17 S. Riha, B. M. Klahr, E. C. Tyo, S. Seifert, S. Vaida, M. J. Pellin, T. W. Hamann and B. F. Martinson, *ACS Nano*, 2013, **7**, 2396.
- 18 L. Badia-Bou, E. Mas-Marza, P. Rodenas, E. M. Barea, F. Fabregat-Santiago, S. Gimenez, E. Peris and J. Bisquert, *J. Phys. Chem. C*, 2013, **117**, 3826.
- 19 I. Thomann, B. A. Pinaud, Z. Chen, B. F. Clemens, T. F. Jaramillo and M. L. Brongersma, *Nano Lett.*, 2011, **11**, 3440.
- 20 H. Gao, C. Liu, H. E. Jeong and P. Yang, *ACS Nano*, 2012, **6**, 234–240.
- 21 B. Iandolo and M. Zäch, *Aust. J. Chem.*, 2012, **65**, 633.
- 22 S. C. Warren and E. Thimsen, *Energy Environ. Sci.*, 2012, **5**, 5133.
- 23 B. Iandolo, T. J. Antosiewicz, A. Hellman and I. Zorić, *Phys. Chem. Chem. Phys.*, 2013, **15**, 4947.
- 24 H. Kausche, *Corrosion of Metals. Physicochemical Principles and Current Problems*, Springer, Berlin, Heidelberg, 2003.
- 25 A. Furube, L. Du, K. Hara, R. Katoh and M. Tachiya, *J. Am. Chem. Soc.*, 2007, **129**, 14852.
- 26 Z. W. Liu, W. B. Hou, P. Pavaskar, M. Aykol and S. B. Cronin, *Nano Lett.*, 2011, **11**, 1111.
- 27 H. M. Chen, C. K. Chen, C. J. Chen, L. C. Cheng, P. C. Wu, B. H. Cheng, Y. Z. Ho, M. L. Tseng, Y. Y. Hsu and T. S. Chan, *ACS Nano*, 2012, **6**, 7362.
- 28 R. Solarska, A. Krolikowska and J. Augustynski, *Angew. Chem., Int. Ed.*, 2010, **49**, 7980.
- 29 H. Fredriksson, Y. Alaverdyan, A. Dmitriev, C. Langhammer, D. S. Sutherland, M. Zäch and B. Kasemo, *Adv. Mater.*, 2007, **19**, 4297.
- 30 B. Seger, A. B. Laursen, P. C. K. Vesborg, T. Pedersen, O. Hansen, S. Dahl and I. Chorkendorff, *Angew. Chem., Int. Ed.*, 2012, **51**, 9128.
- 31 B. S. Yeo and A. T. Bell, *J. Am. Chem. Soc.*, 2011, **133**, 5587.
- 32 A. G. Loomis, Solubilities of gases in water, in *International Critical Tables of Numerical Data, Physics, Chemistry and Technology*, ed. E. W. Washburn, C. J. West, N. E. Dorsey, F. R. Bichowsky and A. Klemenc, McGraw-Hill, Inc., 1928, vol. III, pp. 255–261.